Modeling Control and Simulation of a Series Hybrid Propulsion System

1st Davide Tebaldi
Department of Engineering "Enzo Ferrari"
University of Modena and Reggio Emilia
Modena, Italy
davide.tebaldi@unimore.it

2nd Roberto Zanasi
Department of Engineering "Enzo Ferrari"
University of Modena and Reggio Emilia
Modena, Italy
roberto.zanasi@unimore.it

***Abstract*—This paper deals with the modeling control and simulation of a series hybrid propulsion system for driving a Wheel Loader by relying upon the Power-Oriented Graphs (POG) modeling technique. The considered propulsion system is composed of the following elements: an ICE (Internal Combustion Engine), two controlled PMSMs (Permanent Magnet Synchronous Motors), a supercapacitor as energy storage device and the transmission system of the vehicle itself from the gearbox all the way down to the vehicle wheels. A strategy for the control of the considered hybrid architecture is studied, with the objective of minimizing the ICE specific fuel consumption. Simulation results showing the operation of the presented strategy are finally reported and commented in detail.**

***Index Terms*—Power-Oriented Graphs (POG), Series Hybrid Electric Vehicles (HEVs), Heavy-Duty Vehicles, Graphical Energetic Modeling, Simulation**

I. Introduction

Hybrid electric vehicles (HEVs) are going to occupy a wider and wider slice of modern road transportation, representing a promising solution to reduce air pollution. The first step for the development of a HEV is a well-defined dynamic modeling of the several elements composing the architecture, for which different approaches can be adopted. In [1], the vehicle model is obtained using the Newton's second law of motion. Bond Graphs are used in [2] to analyze the power flow in series and parallel HEVs; whereas EMR (Energetic Macroscopic Representation) is used in [3] to model different vehicles. Bond Graphs and EMR are two graphical modeling techniques exploiting an energetic approach, providing different trade-offs between pros and cons [4]. An energy modeling approach is also used in [5] to provide a unified modeling of HEV drivetrains. In this paper, the Power-Oriented Graphs (POG) technique [6] is employed. The main advantages offered by the POG technique [4] include the generation of a model which is directly implementable in Simulink with no need of additional libraries using standard Simulink blocks, and the straightforward analysis of the system power flows. The main architectures for HEVs include series, parallel and power-split architectures, each having pros and cons with respect to one another. The work presented in this paper addresses the modeling and control of a series hybrid propulsion system for driving a Wheel Loader, with the final objective of making a comparison with other architecture topologies in terms of performances in a future work.

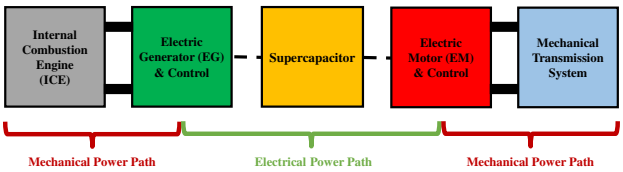

Fig. 1. Structure of the considered series hybrid propulsion system.

Series HEVs are a particular category of hybrid electric vehicles where there is no mechanical coupling between the endothermic engine and the vehicle transmission [7]. A schematic representation of the considered series hybrid architecture is given in Fig. 1, where the electric machine on the left is denoted by EG (working as a generator only) and the one on the right is denoted by EM (either working as a motor or performing energy recovery). The absence of a direct mechanical power path from the ICE to the transmission represents one of the main advantages of series HEVs: the ICE torque and the ICE speed are decoupled from the transmission torque and speed, respectively, and can be exploited as degrees of freedom. The control strategy of a HEV plays an important role in maximizing the benefits. The energy management of series HEVs is addressed in [8] and [9]. In this paper, the control of the considered series HEV is approached by providing a solution for the power management problem handling the ICE, the EG and the EM which is based on the concept of *minimum specific consumption path*, derived on the two-dimensional state space having the ICE torque on the y-axis and the ICE speed on the x-axis. Such concept is introduced in [10] for power-split HEVs, see [11], and is extended in this paper for series HEVs, with the purpose of minimizing the ICE specific fuel consumption of the considered vehicle.

The paper is organized as follows: Sec. II describes the modeling of the considered hybrid system shown in Fig. 1, giving particular focus to the vehicle transmission system. Sec. III describes the underlying concept and the operation of the control strategy for the ICE, the EM and the EG. In Sec. IV, the results of a simulation with reference to an industrial case study are reported and commented. Eventually, the conclusions of this study are reported in Sec. V.

II. Modeling of the Hybrid Vehicle

The structure of the series hybrid architecture studied in this paper is reported in Fig. 1 and the corresponding Simulink block scheme is shown in Fig. 2. From Fig. 1 and Fig. 2, it is possible to appreciate the one-to-one correspondence between the conceptual scheme of the architecture and its Simulink implementation. The elements composing the hybrid architecture in Fig. 2 are, from left to right, the ICE, the EG, the inverter controlling this machine, the supercapacitor playing the role of energy storage device, the inverter controlling the EM, the EM and the mechanical transmission system of the vehicle, i.e. the Wheel Loader, from the gearbox all the way down to the wheels. The red dashed lines present in Fig. 2 denote the power sections connecting the physical elements with each other. Since the product of the two power variables characterizing a power section has the meaning of "power flowing through that section", the power section-based structure of the considered hybrid architecture, typical of POG schemes, allows to maintain an excellent control on the power flows within the system. The employed electric machines, whose modeling has been performed by using the POG technique (see [6] and [12]), are PMSMs. The actual parameters values used in the machines models have been estimated from the machines datasheet by applying an estimation procedure based on a least square algorithm and on the concept of system efficiency, as described by the authors in [13] and [14]. Subsystems "Control of the Electric Generator" and "Control of the Electric Motor" contain the implementation of the vectorial control [15], in order to model the action of the inverters controlling the corresponding electric machines. The simple, one-dimensional model of the supercapacitor used as energy storage device has been represented with the aid of the POG technique. The ICE is modeled as a lookup table representing the maximum motive torque which can be provided by the ICE T_{ice_M} as a function of the ICE speed W_{ice}. The control strategy for this element is based on the concept of *minimum specific consumption path* [10]. The dynamic model of the vehicle transmission system is described in detail in the following Sec. II-A.

A. Dynamic Model of the Vehicle Transmission System

The mechanical transmission model is reported within the subsystem named "Mechanical Dynamics" in Fig. 2. A schematic representation of such system, modeling the transmission from the gearbox all the way down to the wheels, is shown in Fig. 3. The corresponding POG block scheme showing the underlying dynamic model is shown in Fig. 4, from which the state-space model can be directly obtained, see [6].

From Fig. 2 and Fig. 3, the reader can verify that the input power section of the vehicle transmission system, i.e. Section (6), is the one connecting the EM to the transmission system of the vehicle. Indeed, such section is the one representing the input power section for the POG transmission scheme in Fig. 4.

The two power variables characterizing Section (6) are the gearbox input shaft resistive torque T_{m_r}, representing the resistive torque applied to the rotor of the EM, and the angular speed of the gearbox input shaft W_m, which is also the EM angular speed.

Reference is made to Fig. 3 and Fig. 4, where the one-to-one correspondence between the schematic representation of the vehicle transmission and its POG block scheme is highlighted with the aid of a color-based code and the description of the several parts of the transmission is detailed in the following.

The part highlighted in orange is the Gearbox: the connection block characterized by parameters R_g models the gearshifting mechanism and introduces the following relations between the upstream and downstream power variables, as shown in Fig. 4:

$$W'_t = R_g W_m,\ T_{m_r} = R_g T_t \quad \text{where} \quad R_g \in \left\{ \frac{1}{r_1}; \frac{1}{r_2} \right\} \tag{1}$$

Parameters r_1 and r_2 are the gear ratios accounting for the first and second gears, respectively. The torsional spring characterized by stiffness coefficient K_t has been inserted for decoupling purposes, together with the dissipative element d_t in parallel to the spring accounting for the energy loss due to the compression and decompression of the torsional spring, having an impact on the system during the transient.

The part highlighted in lightblue is the Transmission Shaft: the rear and front transmission shafts in Fig. 3 are accounted for together by moment of inertia J_t, and b_t is a friction coefficient introducing a resistive torque which is linearly proportional to the transmission shaft angular speed W_t.

The part highlighted in green is the Differential. The purpose of this element is to distribute the motive torque among the left and right wheels, therefore its contribution can be modeled as a reduction ratio characterized by parameter R_d, together with a decoupling rotational spring K_w and its friction coefficient d_w. Reduction ratio R_d introduces the following relations between the upstream and downstream power variables, as shown in Fig. 4:

$$W'_w = \frac{1}{R_d} W_t, \qquad T'_t = \frac{1}{R_d} T_w \tag{2}$$

The first part highlighted in magenta accounts for the Wheels Dynamics: J_w is the equivalent moment of inertia of the four wheels R_1, R_2, F_1 and F_2, and b_w is a friction coefficient introducing a resistive torque which is linearly proportional to the wheels angular speed W_w.

The second part highlighted in magenta in Fig. 4 accounts for the Wheels radius, in correspondence of which energy conversion from the mechanical rotational to the mechanical translation domain takes place thanks to the connection block accounting for the wheel radius R_r, which introduces the following relations between the upstream and downstream power variables, see Fig. 4:

$$v'_v = R_r W_w, \qquad T'_w = R_r F_v \tag{3}$$

The rotational spring characterized by stiffness coefficient K_v, together with the friction coefficient d_v attached in parallel to it, account for the elasticity of the wheel drive shafts.

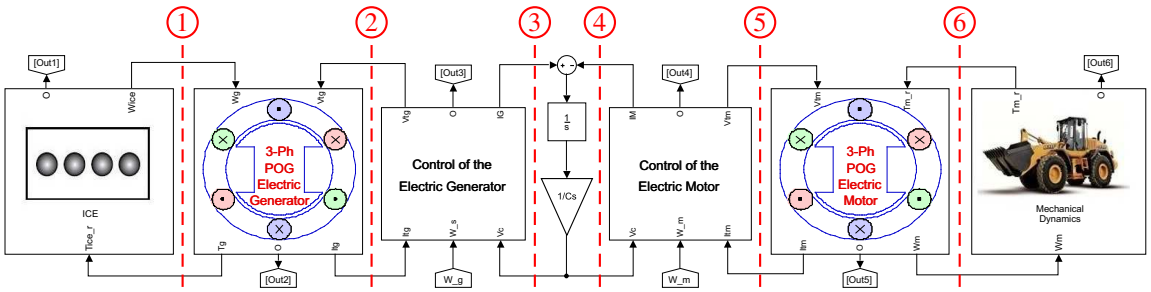

Fig. 2. Simulink block scheme of the considered series hybrid propulsion system.

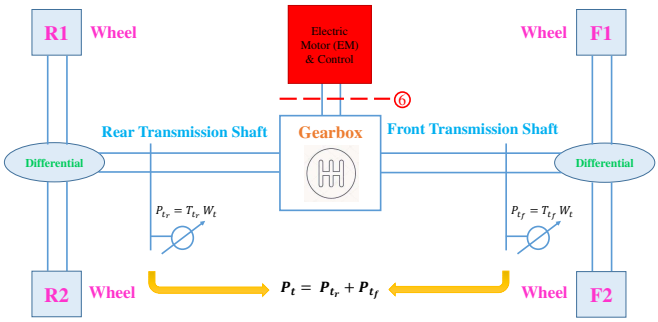

Fig. 3. Structure of the considered vehicle transmission system.

The next part is highlighted in black and describes the Vehicle Dynamics given by the vehicle mass M_v.

The last part of the block scheme in Fig. 4 describes the main external Force Contributions such as, from left to right, the Coulomb friction, the route slope action and the air friction. As far as the Coulomb friction is concerned, the classical modeling as a sign function $F_{a0}\,\mathrm{sign}(v_v)$, where F_{a0} is the modulus of the Coulomb friction and v_v is the vehicle speed, has been replaced by an arctan function: $F_c = \frac{2\,F_{a0}}{\pi}\,\mathrm{atan}(k\,v_v)$. By choosing a rate of change k which is sufficiently high, it is possible to obtain a good approximation of the Coulomb friction with a smoother transition from $-F_{a_0}$ to F_{a_0} and viceversa when the vehicle direction reverses, i.e. when the sign of v_v changes, thus reducing the risk of causing system oscillations. As for the route slope action, the corresponding force is given by $F_s = M_v\,g\,\sin(\alpha)$, where M_v is the vehicle mass, g is the gravitational acceleration, α is the route slope and the resulting F_s is the projection of the vehicle weight force along the vehicle path direction. The air friction is accounted for by formula $F_a = \rho_a\,C_x\,S\,{v_v}^2$, where ρ_a is the air density, C_x is the air penetration coefficient and S is the transverse section of the vehicle. It is worth highlighting that the air friction impact is going to be quite limited in an application such as the one under consideration, as Wheel Loaders are vehicles which are not supposed to travel at high speed.

III. Control Strategy

The proposed solution for the power management problem is described in this section. In the considered architecture, the endothermic power source is the ICE and the two electric power sources are the EM and the EG. The three requirements that must be satisfied are:

- Provide the load with the demanded power level;
- Maintain the supercapacitor voltage within the lower and upper acceptable thresholds;
- Minimize the ICE specific fuel consumption.

By looking at Fig. 1, one can verify that the series structure of the considered architecture eliminates any direct mechanical path from the ICE to the transmission system. From this fact, three important observations can be made:

A) *The ICE speed W_{ice} is decoupled from the gearbox input shaft speed W_m*;
B) *The ICE torque T_{ice} is decoupled from the gearbox input shaft torque T_{m_r}*;
C) *The power demand from the transmission system is fully up to the EM, given by $P_m = W_m\,T_{m_r}$*, as shown in Fig. 2 and Fig. 4.

The control applied to the ICE is based on observations A) and B) and is described in Sec. III-A. The control applied to the EG is based on observation B) and is described in Sec. III-B. The control applied to the EM is based on observation C) and is described in Sec. III-C.

A. Control of the ICE

The decoupling of ICE speed W_{ice} from the gearbox input shaft speed W_t makes it possible to choose the most suitable ICE speed as a function of the ICE demanded power; a PID (Proportional-Intergal-Derivative) regulator is therefore employed to apply a *speed control* to the ICE. The objective of the control strategy is to make the ICE work in the most efficient operating regions of the specific consumption map, where the ICE specific consumption is minimized. Since both the ICE speed W_{ice} and the ICE torque T_{ice} can be exploited as degrees of freedom, according to observations A) and B) in Sec. III, a powerful tool that can be employed is the *ICE minimum specific consumption path*, which allows to determine the most suitable ICE operating point (W_{ice}, T_{ice}), i.e. the one minimizing the specific consumption, as a function of the ICE demanded power. The rules for deriving the *ICE minimum specific consumption path* are described by the authors in [10]-Sec. III.A. The resulting *ICE minimum specific consumption*

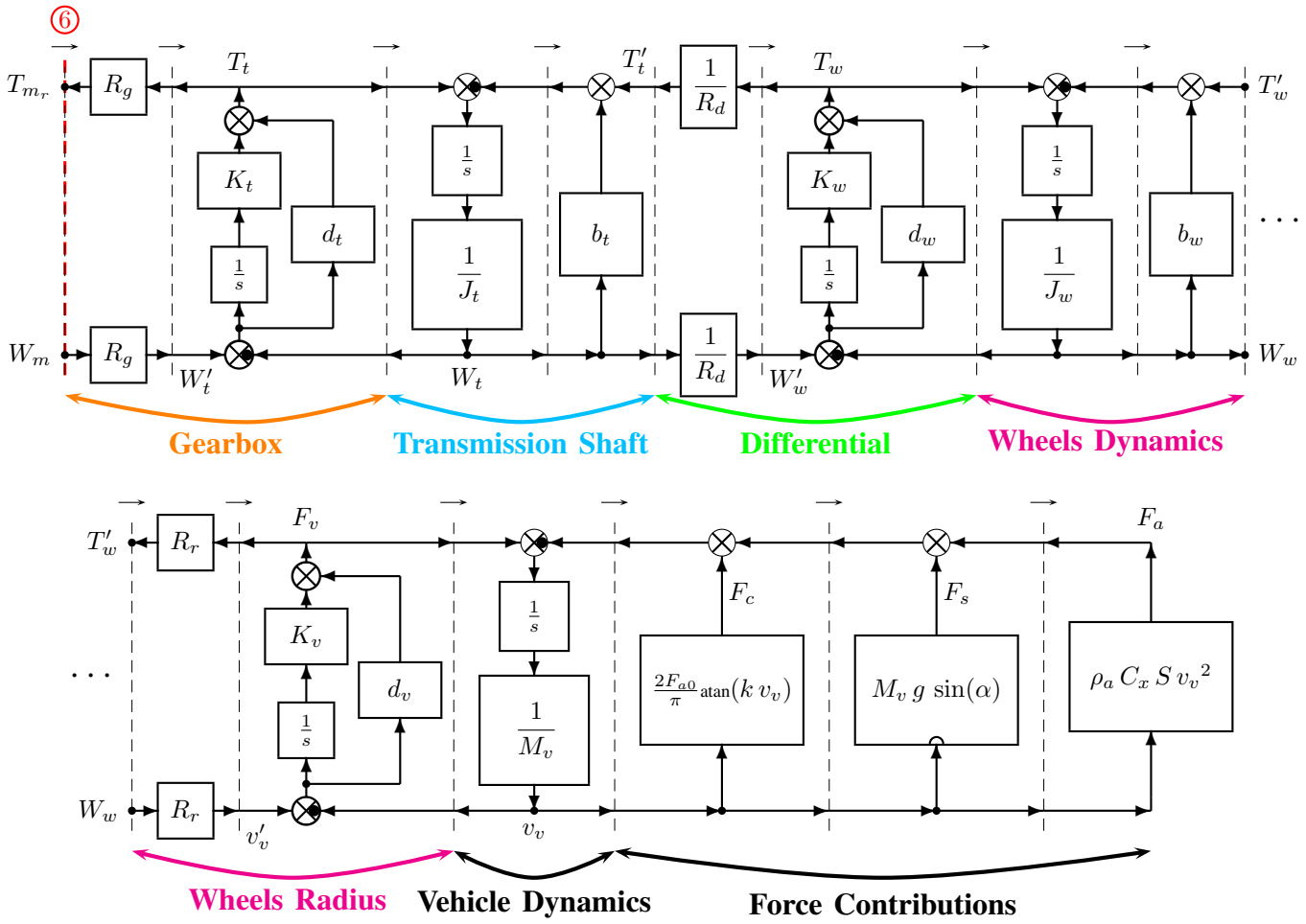

Fig. 4. POG block scheme of the considered vehicle transmission system.

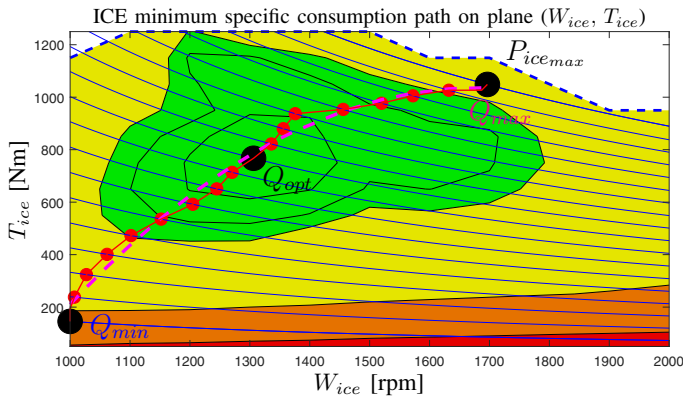

Fig. 5. ICE minimum specific consumption path on the operating plane (W_{ice}, T_{ice}).

path on the ICE operating plane (W_{ice}, T_{ice}) is shown in [10]-Fig. 4 and recalled in Fig. 5 for the sake of clearness. The red curve in Fig. 5 shows the computed *minimum specific consumption path*, whereas the magenta dashed curve in Fig. 5 shows the final smooth *minimum specific consumption path* described by the following second order polynomial function, see [10]-(4):

$$T_{ice} = a_0 + W_{ice} a_1 + W_{ice}^2 a_2, \text{ where } \begin{cases} a_0 = -4.01 \cdot 10^3 \\ a_1 = 57.41 \\ a_2 = -0.16 \end{cases} \quad (4)$$

The most suitable ICE operating point for the ICE is chosen on the *minimum specific consumption path* as a nonlinear function of the voltage drop across the supercapacitor, see [10]-(5):

$$(W_{ice_{des}}, T_{ice_{des}}) = \begin{cases} Q_{opt} & \text{if } V_{c_{low}} < V_c < V_{c_{up}} \\ Q_{req} & \text{if } V_c \le V_{c_{low}} \text{ until } V_c = V_{c_{ref}} \\ Q_{max} & \text{if } V_c \le V_{c_{min}} \text{ until } V_c = V_{c_{ref}} \\ Q_{min} & \text{if } V_c \ge V_{c_{up}} \text{ until } V_c = V_{c_{ref}} \end{cases} \quad (5)$$

where $V_{c_{min}}$, $V_{c_{low}}$, $V_{c_{ref}}$ and $V_{c_{up}}$ are the minimum, lower, reference and upper thresholds of supercapacitor voltage V_c:

$$V_{c_{min}} < V_{c_{low}} < V_{c_{ref}} < V_{c_{up}}, \qquad V_{c_{ref}} = \frac{V_{c_{low}} + V_{c_{up}}}{2}$$

The four operating points Q_{opt}, Q_{req}, Q_{max} and Q_{min}, see [10]-Sec. III.A and [10]-(5), are defined as follows:

$$Q_{opt} = \left(\omega_{ice_{opt}}, \tau_{ice_{opt}}\right), \qquad Q_{req} = \left(\omega_{ice_{req}}, \tau_{ice_{req}}\right),$$

$Q_{max} = (\omega_{ice_{max}}, \tau_{ice_{max}})$, $Q_{min} = (\omega_{ice_{min}}, \tau_{ice_{min}})$

The operating points Q_{opt}, Q_{max} and Q_{min} are present in Fig. 5 and belong to the *minimum specific consumption path* of the ICE. The *required operating point* $Q_{req} = (\omega_{ice_{req}}, \tau_{ice_{req}})$ when $V_c \leq V_{c_{low}}$ is computed as follows, see [10]-Sec. III.A:

1) $\Delta_P = \dfrac{\Delta_E}{\Delta_T} = \dfrac{\frac{1}{2} C_s V_{c_{ref}}^2 - \frac{1}{2} C_s V_{c_{low}}^2}{\Delta_T}$

2) $P_{ice_{req}} = P_{ice_{opt}} + \Delta_P = W_{ice_{opt}} T_{ice_{opt}} + \Delta_P$

3) $W_{ice_{req}} = K P_{ice_{req}}$

4) $T_{ice_{req}} = a_0 + W_{ice_{req}} a_1 + W_{ice_{req}}^2 a_2$

where Δ_P is the ICE required additional power, $\Delta_T = t_{low} - t_{ref}$ is the time interval between the instant t_{low} when $V_c = V_{c_{low}}$ and the instant t_{ref} when $V_c = V_{c_{ref}}$, K is a proportional coefficient properly chosen, and the polynomial used in step 4) is the one defined in (4). Once the desired ICE speed $W_{ice_{des}} \in \{W_{ice_{min}}, W_{ice_{opt}}, W_{ice_{req}}, W_{ice_{max}}\}$ is determined according to (5), the ICE is driven to the desired speed by using the PID regulator.

B. Control of the EG

From Fig. 1, Fig. 2 and Fig. 3, it is evident that the ICE and the EG share the same angular speed $W_{ice} = W_m$ as the ICE shaft and the EG shaft are rigidly connected together. From Sec. III-A it is known that a speed control is applied to the ICE, meaning that the purpose of the control applied to the EG will be to control the remaining power variable: the EG motive torque T_g which is equal to the ICE load torque T_{ice_l}, see Fig. 2, in agreement with observation B) in Sec. III. The ICE desired torque $T_{ice_{des}} \in \{T_{ice_{min}}, T_{ice_{opt}}, T_{ice_{req}}, T_{ice_{max}}\}$ is determined by the nonlinear function (4) and, according to the previous observations, also represents the EG desired torque:

$$T_{g_{des}} = T_{ice_{des}} \tag{6}$$

The desired torque $T_{g_{des}}$ is then imposed to the EG by means of the inverter implementing the vectorial control, i.e. subsystem "Control of the Electric Generator" reported in Fig. 2.

C. Control of the EM

According to observation C) in Sec. III, the power demand from the transmission system must be fully satisfied by the EM. From this observation, it follows that a *speed control* has to be applied to the EM, in order to make it follow the desired speed profile $W_{m_{des}}$, which is directly proportional to the vehicle desired speed profile $v_{v_{des}}$ according to (1), (2) and (3):

$$W_{m_{des}} = \frac{R_d}{R_r R_g} v_{v_{des}} \tag{7}$$

A PID regulator is then used in order to convert the speed tracking error $W_{m_{des}} - W_m$ into a desired torque $T_{m_{des}}$ for the EM, which is responsible for compensating the transmission system resistive torque T_{m_r}, see Fig. 4.

The desired torque $T_{m_{des}}$ is then imposed to the EM by means of the inverter implementing the vectorial control, i.e. subsystem "Control of the Electric Motor" reported in Fig. 2.

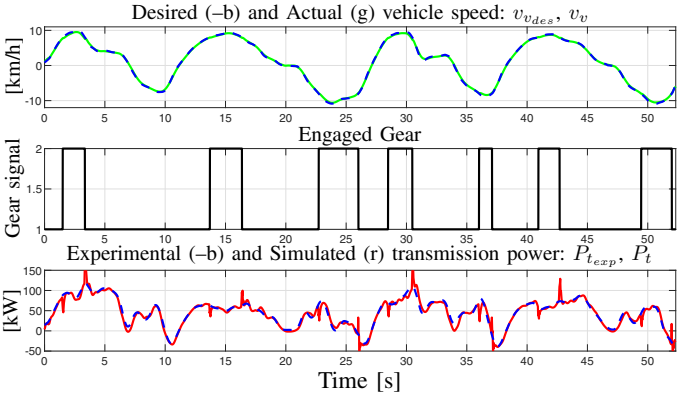

Fig. 6. Desired and Actual Vehicle Speed; Gear; Transmission power.

IV. Simulations

The considered architecture reported in Fig. 2 has been simulated with reference to an industrial case study: the goal of the simulation is to make the vehicle follow a desired speed profile $v_{v_{des}}$ when the most significant friction contributions acting on the system are:

1) The Coulomb friction;
2) An external resistive force profile.

The actual values of the model parameters could not be reported because of industrial secret reasons. The external resistive force profile is responsible for simulating the resistive force that the transmission system is subject to when the Wheel Loader is either digging (i.e. loading the bucket) or unloading the bucket. The total resistive force applied to the vehicle $F_{t_{exp}}$ is therefore given by the two contributions 1) and 2) reported above and has been acquired by experimental measurements performed on the field for the analyzed cycle. The corresponding load power $P_{t_{exp}}$ is absorbed by the rear and front transmission shafts in order to make the vehicle follow the desired speed profile $v_{v_{des}}$ when the total experimental resistive force $F_{t_{exp}}$ is applied to the vehicle. In the considered hybrid architecture, such power $P_{t_{exp}}$ must be fully provided by the EM, see Sec. III-C. In this simulation, the vehicle is supposed to be working on a plane route, meaning that the route slope external force contribution has no impact. Additionally, the air friction is neglected because of the low traveling speed of the Wheel Loader.

The obtained simulation results are shown in Fig. 6, Fig. 7, Fig. 8, Fig. 9 and Fig. 10. The upper subplot of Fig. 6 shows the desired speed profile $v_{v_{des}}$ that the vehicle is required to follow (blue dashed curve) and the actual vehicle speed v_v (green curve). The middle subplot of Fig. 6 shows the currently engaged gear, which upshifts from $R_g = 1/r_1$ to $R_g = 1/r_2$ when the absolute value of the vehicle speed

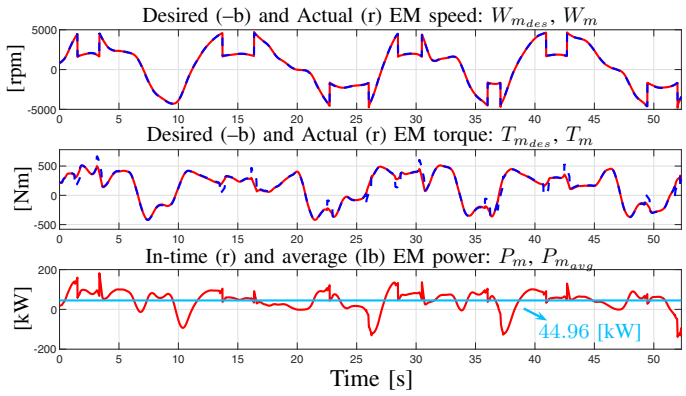

Fig. 7. EM: Desired and Actual Speed; Desired and Actual torque; In-time and average power.

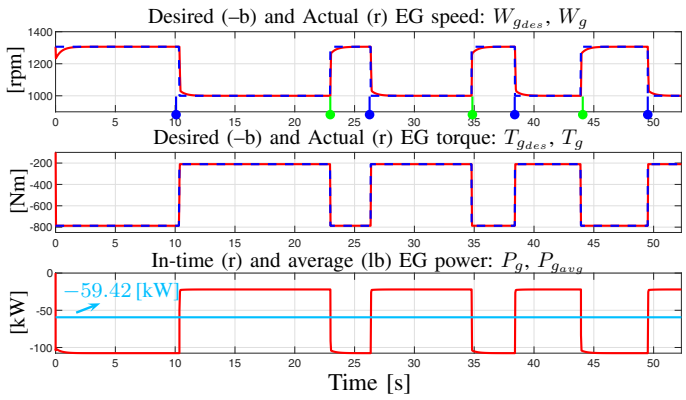

Fig. 8. EG: Desired and Actual Speed; Desired and Actual torque; In-time and average power.

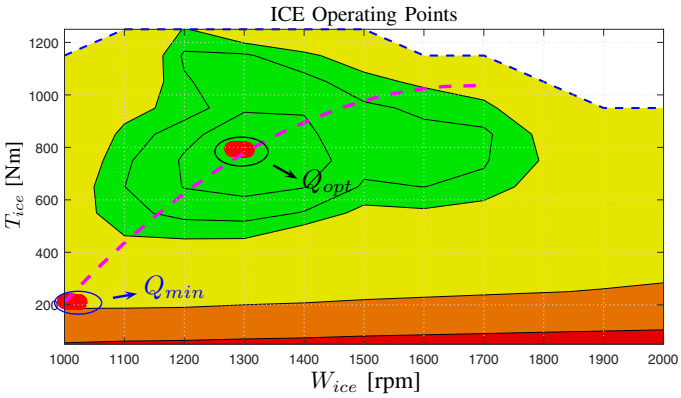

Fig. 9. ICE operating points and ICE minimum specific consumption path on the specific consumption map.

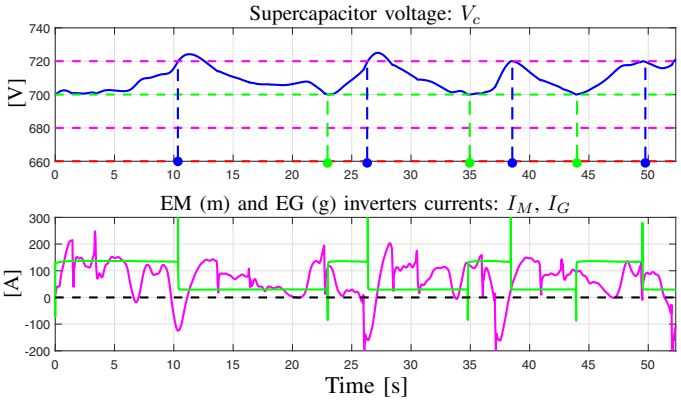

Fig. 10. Supercapacitor voltage; Currents from the inverters.

overtakes the threshold of 8 [km/h] and viceversa. The lower subplot of Fig. 6 shows the total transmission power $P_{t_{exp}}$ acquired from experimental data on the field during the given cycle (blue dashed curve) and the transmission power P_t from the simulation (red curve): the good matching between $P_{t_{exp}}$ and P_t denotes the effectiveness of the control applied on the EM, allowing to fully satisfy the power demand from the transmission.

Fig. 7 shows the desired EM speed profile $W_{m_{des}}$ (blue dashed curve), which is computed from the desired vehicle speed profile $v_{v_{des}}$ according to (7), and the actual EM speed W_m (red curve) in the upper subplot. From the middle subplot of Fig. 7, it is possible to see the desired torque $T_{m_{des}}$ for the EM in order to follow the desired speed profile $W_{m_{des}}$ and the actual EM torque T_m. The good matching between the desired and actual speed and torque characteristics furthermore denotes the effectiveness of the speed control applied to the EM, allowing to satisfy the power demand coming from the load, i.e. the transmission. The lower subplot of Fig. 7 shows the power profile P_m generated by the EM (red curve) and the average value of such power $P_{m_{avg}}$ (light blue line).

The upper subplot of Fig. 8 shows the EG desired speed, which coincides with the ICE desired speed $W_{g_{des}} = W_{ice_{des}}$, and the actual EG and ICE speed $W_g = W_{ice}$: the good matching between the two characteristics highlights the effectiveness of the speed control applied to the ICE. The blue markers identify the time instants at which the supercapacitor voltage becomes greater than the upper threshold $V_c > V_{c_{up}}$, in correspondence of which the EG and ICE speed is set from the initial optimal value $W_g = W_{ice} = W_{ice_{opt}}$ down to the minimum value $W_g = W_{ice} = W_{ice_{min}}$ in order not to overcharge the supercapacitor according to (5). The green markers identify the time instants at which the decreasing supercapacitor voltage V_c reaches the reference value $V_{c_{ref}}$, in correspondence of which the EG and ICE speed is newly set to the optimal one $W_g = W_{ice} = W_{ice_{opt}}$. The middle subplot of Fig. 8 shows the EG desired torque $T_{g_{des}}$ (blue dashed curve), given by (5) and (6), and the actual EG torque T_g (red curve). The latter T_g also represents the load torque T_{ice_l} applied to the ICE, see Fig. 2, which has to be counteracted by the ICE motive torque T_{ice} in order to maintain the desired ICE speed $W_{ice_{des}}$. The good matching between the two desired and actual torque characteristics $T_{g_{des}}$ and T_g shows the effectiveness of the torque control applied to the EG, whose purpose is to ensure that the condition $T_{ice} = T_{ice_{des}}$

is always verified, thus confining the ICE operating point on the *minimum specific consumption path*. The lower subplot of Fig. 8 shows the power profile P_g of the EG (red curve), which is negative because the machine acts as a generator, and the average value of such power $P_{g_{avg}}$ (light blue line).

The ICE operating points are marked by the red dots in Fig. 9, showing the ICE specific consumption map on the operating plane (W_{ice}, T_{ice}). From this figure one can notice that, under the current simulation conditions, the ICE operating point is either equal to the optimal one $Q_{ice} = Q_{opt}$ or to the minimum one $Q_{ice} = Q_{min}$. This well agrees with the following observation: with reference to the third subplots of Fig. 7 and Fig. 8, it is possible to verify that the average EM power $P_{m_{avg}}$, and thus the average transmission power $P_{t_{avg}}$, are lower than the modulus of the average ICE and EG power $P_{g_{avg}}$ in the considered operating points $Q_g = Q_{ice} \in \{Q_{min}, Q_{opt}\}$. This explains why, *under the considered simulation conditions*, there is no need for the ICE to work in the operating points $\{Q_{req}, Q_{max}\}$, since the generated power would be much higher than the one absorbed by the transmission. Metrics providing the reduction of the ICE specific fuel consumption with respect to the traditional non-hybrid Wheel Loader could not be provided because of industrial secret reasons.

Fig. 10 shows the voltage drop across the supercapacitor in the upper subplot (blue curve) and the considered thresholds $V_{c_{min}}$, $V_{c_{low}}$,$V_{c_{ref}}$ and $V_{c_{up}}$ introduced in (5) in red, magenta, green and magenta dashed lines, respectively. The meaning of the blue and green markers is the same as in Fig. 8.

The lower subplot of Fig. 10 shows the EG inverter current I_G (green curve) always recharging the supercapacitor ($I_G > 0$), and the EM inverter current I_M (magenta curve), either discharging ($I_M > 0$) or recharging ($I_M < 0$) the supercapacitor depending on the Wheel Loader operating conditions. The discrimination about whether the EM and the EG are recharging or discharging the supercapacitor can be made on the basis of the EG and EM inverter currents I_G and I_M by carefully looking at the summation node at the input of the supercapacitor shown in Fig. 2. Since the EG inverter current I_G enters the supercapacitor input summation node with a "+" sign, whereas the EM inverter current I_M enters the supercapacitor input summation node with a "-" sign, it follows that:

$$\begin{cases} I_M > 0 \quad \Rightarrow \quad \text{EM discharging the supercapacitor } \checkmark \\ I_M < 0 \quad \Rightarrow \quad \text{EM recharging the supercapacitor } \checkmark \\ I_G > 0 \quad \Rightarrow \quad \text{EG recharging the supercapacitor } \checkmark \\ I_G < 0 \quad \Rightarrow \quad \text{EG discharging the supercapacitor } \otimes \end{cases}$$

Note that the last case $(I_G < 0)$ can never happen, as in the considered architecture the EG cannot work as a motor, since the ICE cannot absorb power. As regards the condition $I_M < 0$, the time frames in which the EM does contribute to *recharge* the supercapacitor are those in which the vehicle is required to decelerate: the braking action is performed with the aid of the EM and energy recovery takes place. The potentiality of performing this latter operation is one of the main advantages of Hybrid Electric Vehicles.

V. Conclusions

In this paper, the modeling and control of a series hybrid architecture have been analyzed. By using the POG technique, the modeling of all the physical elements composing the considered hybrid architecture has been performed. As regards the control, an effective solution for the power management problem has been given, allowing to satisfy all the requirements: guarantee the load demanded power level, maintain the supercapacitor state of charge within the acceptable thresholds and minimize the ICE specific fuel consumption. The proposed control strategy has finally been tested with the aid of some simulation results, thus proving its effectiveness for controlling the presented hybrid propulsion system.

References

[1] M. Ducusin, S. Gargies, and C. Mi, "Modeling of a series hybrid electric high-mobility multipurpose wheeled vehicle", IEEE Transactions on Vehicular Technology, vol. 56, no. 2, pp. 557-565, Mar.2007.

[2] M. Cipek, J. Deur, J. Petrić, "Bond Graph Analysis of Power Flow in Series-Parallel Hybrid Electric Vehicle Transmissions", UKACC International Conference on Control, Coventry, UK, September 7-10, 2010.

[3] K. Chen, A. Bouscayrol, A. Berthon, P. Delarue, D. Hissel, R. Trigui, "Global modeling of different Vehicles Using Energetic Macroscopic Representation", IEEE Vehicle Power and Propulsion Conference (VPPC), Harbin, China, September 3-5, 2008.

[4] R. Zanasi, G. H. Geitner, A. Bouscayrol, W. Lhomme, "Different energetic techniques for modelling traction drives", 9th Internation Conference on Modeling and Simulation of Electric Machines, Converters and Systems (ELECTRIMACS), Québec, Canada, June 8-11, 2008.

[5] G. Rizzoni, L. Guzzella, B. M. Baumann, "Unified Modeling of Hybrid Electric Vehicle Drivetrains", IEEE/ASME Transactions on Mechatronics, vol. 4, no. 3, September 2008.

[6] R. Zanasi, "The Power-Oriented Graphs Technique: system modeling and basic properties", IEEE Vehicle Power and Propulsion Conference, Lille, France, September 1-3, 2010.

[7] A. Zia, "A comprehensive overview on the architecture of Hybrid Electric Vehicles (HEV)", 19th International Multi-Topic Conference (INMIC),Islamabad, Pakistan, December 5-6, 2016.

[8] N. Jalil, N. A. Kheir, M. Salman, "A Rule-Based Energy Management Strategy for a Series Hybrid Vehicle", Proceedings of American Control Conference (ACC), Albuquerque, New Mexico, June, 1997.

[9] S. H. Mahyiddin, M. R. Mohamed, Z. Mustaffa, A. C. Khor, M. H. Sulaiman, H. Ahmad, S. Abdul Rahman, "Fuzzy logic energy management system of series hybrid electric vehicle", 4th IET Clean Energy and Technology Conference (CEAT), Kuala Lumpur, Malaysia, November 14-15, 2016.

[10] D. Tebaldi, R. Zanasi, "Modeling and Control of a Power-Split Hybrid Propulsion System", IEEE 45th Annual Conference of the Industrial Electronics Society, Lisbon, Portugal, October 14-17, 2019.

[11] J. M. Miller, "Hybrid electric vehicle propulsion system architectures of the e-CVT type", IEEE Transactions on Power Electronics, vol. 21, no. 3, pp. 756-767, May 2006.

[12] M. Fei, R. Zanasi, F. Grossi, "Modeling of Multi-phase Permanent Magnet Synchronous Motors under Open-phase Fault Condition", 9th IEEE International Conference on Control and Automation (ICCA), Santiago, Chile, December 19-21, 2011.

[13] R. Zanasi, D. Tebaldi, "Power Flow Efficiency of Linear and Nonlinear Physical Systems", 18th IEEE European Control Conference (ECC), Naples, Italy, June 25-28, 2019.

[14] R. Zanasi, D. Tebaldi, "Study of the Bidirectional Efficiency of Linear and Nonlinear Physical Systems", IEEE 45th Annual Conference of the Industrial Electronics Society, Lisbon, Portugal, October 14-17, 2019.

[15] R. Zanasi, F. Grossi, "Vectorial Control of Multi-phase Synchronous Motors using POG Approach", IEEE 35th Annual Conference of the Industrial Electronics Society, Porto, Portugal, November 3-5, 2009.